INTERNATIONAL JOURNAL FOR NUMERICAL METHODS IN FLUIDS
Int. J. Numer. Meth. Fluids 2010; **62**:1063–1080
Published online 9 April 2009 in Wiley InterScience (www.interscience.wiley.com). DOI: 10.1002/fld.2052

Numerical implementation of Aristov–Pukhnachev's formulation for axisymmetric viscous incompressible flows

N. P. Moshkin[1,*,†], K. Poochinapan[1] and C. I. Christov[2]

[1]*School of Mathematics, Suranaree University of Technology, Nakhon Ratchasima, Thailand*
[2]*Department of Mathematics, University of Louisiana at Lafayette, Lafayette, U.S.A.*

SUMMARY

In the present work a finite-difference technique is developed for the implementation of a new method proposed by Aristov and Pukhnachev (*Doklady Phys.* 2004; **49**(2):112–115) for modeling of the axisymmetric viscous incompressible fluid flows. A new function is introduced that is related to the pressure and a system similar to the vorticity/stream function formulation is derived for the cross-flow. This system is coupled to an equation for the azimuthal velocity component. The scheme and the algorithm treat the equations for the cross-flow as an inextricably coupled system, which allows one to satisfy two conditions for the stream function with no condition on the auxiliary function. The issue of singularity of the matrix is tackled by adding a small parameter in the boundary conditions. The scheme is thoroughly validated on grids with different resolutions.

The new numerical tool is applied to the Taylor flow between concentric rotating cylinders when the upper and lower lids are allowed to rotate independently from the inner cylinder, while the outer cylinder is held at rest. The phenomenology of this flow is adequately represented by the numerical model, including the hysteresis that takes place near certain specific values of the Reynolds number. Thus, the present results can be construed to demonstrate the viability of the new model. The success can be attributed to the adequate physical nature of the auxiliary function. The proposed technique can be used in the future for in-depth investigations of the bifurcation phenomena in rotating flows. Copyright © 2009 John Wiley & Sons, Ltd.

Received 6 March 2008; Revised 15 January 2009; Accepted 23 February 2009

KEY WORDS: finite-difference scheme; incompressible viscous fluid; axisymmetric flows

1. INTRODUCTION

Axisymmetric rotating flows have been studied for a variety of reasons. Their technological applications are many (e.g. centrifugal pumps, cyclone separators). Their importance in geophysics is

*Correspondence to: N. P. Moshkin, School of Mathematics, Suranaree University of Technology, Nakhon Ratchasima, Thailand.
†E-mail: moshkin@math.sut.ac.th

Copyright © 2009 John Wiley & Sons, Ltd.

demonstrated over a large range of scales (e.g. tornadoes, hurricanes, ocean circulations). Axisymmetric rotating flows occur past axisymmetric bodies, in axisymmetric jets, etc. A well-studied example is the flow between concentric cylinders where the inner cylinder rotates, which is commonly called the Taylor–Couette problem. The transition from a purely azimuthal Couette flow to a flow with secondary streaming exhibiting cellular Taylor vortexes has been recognized as a cornerstone of the hydrodynamic stability theory. In addition, the problem of the onset of Taylor vortices in a viscous fluid contained between concentric rotating cylinders is an excellent benchmark problem for axisymmetric flows.

When the lids and the cylinders of the Taylor–Couette flow are allowed to rotate at different angular speeds, the phenomenology of the flow becomes very rich and different flow regimes can take place in the wake of the bifurcation phenomenon. In series of works [1–3], the mechanism of vortex breakdown in swirling flows is studied and a comparison between experimental visualization and numerical simulations is presented. The bifurcation for differential rotation of the lids is extensively studied also in [4].

A new form of the Navier–Stokes equations (NSEs) for the axisymmetric motion of a viscous incompressible fluid was proposed by Aristov and Pukhnachev [5] who introduced a new function related to the pressure and succeeded in deriving a coupled system of two elliptic equations for the stream function and the new function. This system is coupled to the equation for the azimuthal velocity component. Mathematically, this formulation resembles the stream function/vorticity formulation but the physical meaning of the coupling function is different. The new formulation offers the possibility to create a different numerical model, which is the main purpose of the present paper. Because of the physical nature of the coupling function, the model may have different mathematical properties than the vorticity/stream function formulation. It can serve both as a validation of the known numerical solutions, and for future in-depth investigation of the bifurcation phenomena in rotating flows.

The paper is organized as follows. Section 2 presents the new set of governing equations of motion as given in [5]. Section 3 gives the geometry of the flow. Section 4 is devoted to the description of the numerical scheme and algorithm we propose for the model from [5]. Further, a thorough validation of the scheme is performed through a detailed comparison with the available numerical and experimental data (see [6]). Section 5 presents the results obtained with the proposed numerical model for several characteristic cases where the flow is very sensitive to small changes of the governing parameters and the quality of the numerical model is of prime importance. We elucidate the impact of the relative angular speeds of the lids and of the aspect ratio on the route to bifurcation and the specific patterns of the flow. Special attention is paid for obtaining accurate results on the hysteresis of the flow that takes place with the increase and decrease in the Reynolds number. Finally, Section 6 summarizes the results of the paper.

2. ARISTOV–PUKHNACHEV FORMULATION

Traditionally, axisymmetric rotating flows have been treated by representing NSEs in cylindrical coordinates. The stream function, stream function/vorticity, or (alternatively) the velocity and pressure fields can be used. An intensive body of the literature exists on the numerical simulation of Taylor–Couette flow. Here, we discuss a modification of the governing equations proposed in [5]. To make this paper self-contained, we present the derivation of the new formulation. First,

Copyright © 2009 John Wiley & Sons, Ltd.

DOI: 10.1002/fld

we write the axisymmetric NSEs in cylindrical polar coordinate system (r, θ, z):

$$u_t + uu_r + wu_z - \frac{v^2}{r} = -p_r + \nu\left(u_{rr} + \frac{1}{r}u_r - \frac{1}{r^2}u + u_{zz}\right) \tag{1}$$

$$v_t + uv_r + wv_z + \frac{uv}{r} = \nu\left(v_{rr} + \frac{1}{r}v_r - \frac{1}{r^2}v + v_{zz}\right) \tag{2}$$

$$w_t + uw_r + ww_z = -p_z + \nu\left(w_{rr} + \frac{1}{r}w_r + w_{zz}\right) \tag{3}$$

$$u_r + \frac{u}{r} + w_z = 0 \tag{4}$$

where u, v, and w are the radial, the azimuthal, and the axial velocity components, respectively, p is the pressure, and ν is the kinematic viscosity. Without loss of generality, the fluid density is taken to be equal to unity, and the fluid is subjected to the potential external forces. In terms of the stream function ψ

$$u = -\frac{1}{r}\psi_z, \quad w = \frac{1}{r}\psi_r \tag{5}$$

Equation (3) yields

$$\frac{\partial}{\partial r}\left(\psi_t - \frac{1}{r}\psi_r\psi_z - \nu E\psi\right) + \frac{\partial}{\partial z}\left(rp + \frac{1}{r}\psi_r^2\right) = 0$$

where

$$E \stackrel{\text{def}}{=} \frac{\partial^2}{\partial r^2} - \frac{1}{r}\frac{\partial}{\partial r} + \frac{\partial^2}{\partial z^2}$$

The key element of the formulation of Aristov and Pukhnachev [5] is that there exists a function Φ that satisfies the relations

$$p = -\frac{1}{r^2}\psi_r^2 + \frac{1}{r}\Phi_r \tag{6}$$

$$\psi_t - \frac{1}{r}\psi_r\psi_z + \Phi_z = \nu E\psi \tag{7}$$

The substitution of Equation (5) into Equation (2) yields

$$J_t - \frac{1}{r}\psi_z J_r + \frac{1}{r}\psi_r J_z = \nu E J \tag{8}$$

where $J = rv$. Upon differentiating Equation (6) with respect to r, Equation (7)—with respect to z, and substituting the result into Equation (1), one obtains

$$E\Phi = \frac{1}{r^2}\left(J^2 + \psi_z^2\right) + \frac{2}{r}\psi_r E\psi \tag{9}$$

The aim of the present work is to develop and validate a finite-difference scheme for the approximate solution of Equations (7)–(9). Below, we will consider only the case where no-slip

Copyright © 2009 John Wiley & Sons, Ltd.

DOI: 10.1002/fld

conditions are prescribed at the boundary of the flow domain. In term of the functions ψ and J, these conditions read as

$$\frac{\partial\psi}{\partial n}=0, \quad \psi=0, \quad J=\Omega r^2 \tag{10}$$

where $\partial\psi/\partial n$ stands for the derivative in the direction of the normal vector to the boundary, Ω is the rate of rotation of boundary surfaces. To complete the formulation of the problem, it is necessary to specify the initial conditions

$$\psi=\psi_0(r,z), \quad J=J_0(r,z), \quad t=0 \tag{11}$$

Equation (8) and boundary condition (10) for J can be effectively decoupled and solved independently assuming that ψ is known. The main difficulty in solving the system of equations for ψ and Φ is that two boundary conditions are specified for ψ while none is available for Φ. This difficulty is similar to the vorticity–stream function equations in two dimensions. To overcome the difficulty caused by the absence of boundary condition for Φ, the authors of [5] transform equation (9) into a fourth-order equation by applying the operator E and using the boundary condition $\partial\psi/\partial n=0$. Then, the boundary conditions for functions ψ and Φ are uncoupled and iterative solution procedures can be used to find approximate solution. The weak point of such an approach is the necessity to solve the Neumann problem for the bi-harmonic equation. The uncoupled solution of this problem can be found up to an arbitrary function, which satisfies the equation $E\widetilde{\Phi}=0$. Here, in order to avoid the Neumann boundary value problem, we propose to solve the system as it stands, without further manipulation.

3. THE FEATURING EXAMPLE

The Taylor–Couette flow provides a unique opportunity for a detailed comparison between the results of experimental and numerical investigations because it is one of the best studied axisymmetric viscous flows. Following [6] we consider a variant of the standard Taylor–Couette flow, in which the lids can rotate independently from the inner cylinder. A schematic of the flow geometry is shown in Figure 1 where the parameters are defined. R_i is the radius of the inner cylinder, R_o is the radius of the outer cylinder, L is the axial length (height), Ω_i is the angular velocity of the inner cylinder, Ω_e is the angular velocity of the lower lid, and Ω_u is the angular velocity of the upper lid. If $\Omega_\mathrm{u}=0$, then we have the case when the upper lid is at rest. For a rotating upper lid, we have $\Omega_\mathrm{u}=\Omega_\mathrm{e}$.

The non-dimensional parameters of the problem are

$$Re=\frac{DR_\mathrm{i}\Omega_\mathrm{i}}{\nu}, \quad \Omega=\frac{\Omega_\mathrm{e}}{\Omega_\mathrm{i}}, \quad \Gamma=\frac{L}{D}, \quad \eta=\frac{R_\mathrm{o}}{R_\mathrm{i}}, \quad D=R_\mathrm{o}-R_\mathrm{i} \tag{12}$$

where Re is the Reynolds number based on the angular speed of the inner cylinder. We do not need a special dimensionless parameter for the upper lid rotation, because it will be either zero or equal to the lower lid. Then the system of Equations (7)–(9) can be made dimensionless by introducing the new variables

$$\hat{r}=\frac{r}{D}, \quad \hat{z}=\frac{z}{D}, \quad \hat{t}=\frac{t\nu}{D^2}, \quad \hat{J}=\frac{J}{\nu}, \quad \hat{\psi}=\frac{\psi}{\nu D}, \quad \hat{\Phi}=\frac{\Phi}{\nu^2} \tag{13}$$

Copyright © 2009 John Wiley & Sons, Ltd.

DOI: 10.1002/fld

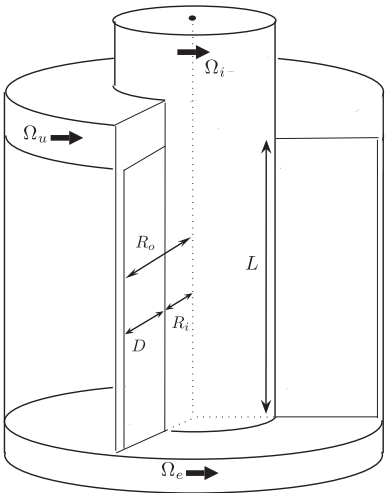

Figure 1. Sketch of the flow domain.

where the gap width D is used as the length scale, and the diffusion time across the gap, $D^2\nu^{-1}$—as the time scale.

4. DIFFERENCE SCHEME AND VALIDATIONS

A plethora of numerical approaches to the Taylor–Couette flow is available in the literature. We mention a few here. In [7], the governing equations are solved by a finite-difference method using the stream function–vorticity formulation. The equations are discretized using second-order accurate central differences and are time stepped using a combination of second-order accurate Crank–Nicolson and Adam–Bashfort methods. In [8], the NSEs are solved using a finite-volume method based on the `SIMPLE` algorithm. The `QUICK` scheme is used for the convective terms. The finite-element package `ENTWINE` is applied to the steady axisymmetric NSEs in [6, 9–11]. We create in this section, a difference scheme and algorithm for the formulation of [5] and compare the results with the mentioned known numerical works.

We cover the non-dimensional domain

$$Q=\left\{\frac{1}{\eta-1}<r<\frac{\eta}{\eta-1},0<z<\Gamma\right\}$$

with a uniform staggered grid

$$Q_h=\left\{(r_i,z_j)|r_i=\frac{1}{\eta-1}+(i-1.5)h_r,z_j=(j-1.5)h_z,i=1,\ldots,N_r,j=1,\ldots,N_z\right\}$$

(see Figure 2) with spacings

$$h_r=\frac{1}{N_r-2},\quad h_z=\frac{\Gamma}{N_z-2}$$

Copyright © 2009 John Wiley & Sons, Ltd.

DOI: 10.1002/fld

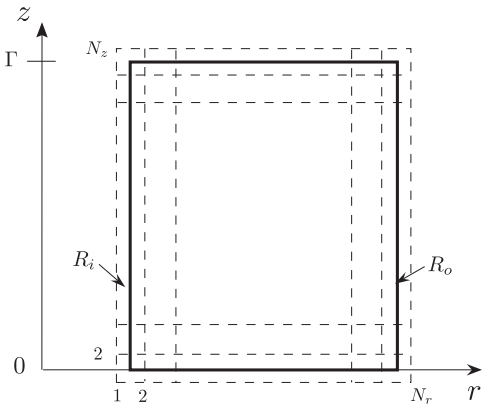

Figure 2. The computational domain with the grid.

in the r- and z-directions, respectively. Such grid allows one to use central differences to approximate the boundary conditions with second order on two-point stencils. In addition, the different functions of the system are staggered in time, which allows us to effectively decouple the equation for the azimuthal velocity J from the equations for the secondary streaming in the cross section (ψ and Φ).

We begin with Equation (8) for the function J, which is approximated at the half-time steps. We use the following Crank–Nicolson scheme:

$$\begin{aligned}\frac{J_{i,j}^{n+1/2}-J_{i,j}^{n-1/2}}{\tau} &= \frac{1}{8r_ih_rh_z}(\psi_{i,j+1}^{n}-\psi_{i,j-1}^{n})(J_{i+1,j}^{n+1/2}-J_{i-1,j}^{n+1/2}+J_{i+1,j}^{n-1/2}-J_{i-1,j}^{n-1/2})\\ &\quad -\frac{1}{8r_ih_rh_z}(\psi_{i+1,j}^{n}-\psi_{i-1,j}^{n})(J_{i,j+1}^{n+1/2}-J_{i,j-1}^{n+1/2}+J_{i,j+1}^{n-1/2}-J_{i,j-1}^{n-1/2})\\ &\quad +\frac{1}{2}(EJ_{i,j}^{n+1/2}+EJ_{i,j}^{n-1/2}) \quad \text{for } i=2,\ldots,N_r-1,\quad j=2,\ldots,N_z-1 \end{aligned} \tag{14}$$

We use the notation

$$EJ_{i,j}=\frac{J_{i+1,j}-2J_{i,j}+J_{i-1,j}}{h_r^2}-\frac{J_{i+1,j}-J_{i-1,j}}{2r_ih_r}+\frac{J_{i,j+1}-2J_{i,j}+J_{i,j-1}}{h_z^2} \tag{15}$$

The boundary conditions are approximated as follows:

$$\begin{aligned}&\frac{J_{1,j}^{n+1/2}+J_{2,j}^{n+1/2}}{2}=\frac{Re}{\eta-1}, \quad \frac{J_{N_r-1,j}^{n+1/2}+J_{N_r,j}^{n+1/2}}{2}=0, \quad j=1,\ldots,N_z\\ &\frac{J_{i,1}^{n+1/2}+J_{i,2}^{n+1/2}}{2}=Re(\eta-1)\Omega r_i^2, \quad \frac{J_{i,N_z-1}^{n+1/2}+J_{i,N_z}^{n+1/2}}{2}=Re(\eta-1)\Omega\Omega_{\mathrm{u}}r_i^2, \quad i=1,\ldots,N_r\end{aligned} \tag{16}$$

Here, we use the notation Ω_{u} to treat the two main cases in a unified manner. If $\Omega_{\mathrm{u}}=0$, then we have the case when the upper lid is at rest. For a rotating upper lid, we have $\Omega_{\mathrm{u}}=1$.

Copyright © 2009 John Wiley & Sons, Ltd.

DOI: 10.1002/fld

We use the standard routines DGBSV and DGBSVX from LAPACK for the numerical solution of the algebraic system. The essential element of the proposed algorithm is that Equations (7) and (9) for ψ and Φ are considered as a coupled system. Note that ψ and Φ are evaluated on the full-time steps. This formulation is based on the idea of regarding the two boundary conditions for ψ as the actual conditions for the $\psi-\Phi$ system. The approach is akin to the conjugate algorithm for stream function/vorticity formulation from [12] and to the one for the primitive variables from [13]. We tackle the boundary conditions in a fully implicit manner through special rearrangement of the values of the unknown functions.

We employ second-order central-difference approximations for the operators in Equations (7) and (9). The system of difference equations is

$$\frac{\psi_{i,j}^{n+1}-\psi_{i,j}^{n}}{\tau}-\frac{(\psi_{i+1,j}^{n}-\psi_{i-1,j}^{n})(\psi_{i,j+1}^{n+1}-\psi_{i,j-1}^{n+1})+(\psi_{i+1,j}^{n+1}-\psi_{i-1,j}^{n+1})(\psi_{i,j+1}^{n}-\psi_{i,j-1}^{n})}{8r_i h_r h_z}$$
$$+\frac{(\Phi_{i,j+1}^{n+1}-\Phi_{i,j-1}^{n+1})}{2h_z}=\frac{1}{2}(E\psi_{i,j}^{n+1}+E\psi_{i,j}^{n}) \tag{17}$$

$$E\Phi_{i,j}^{n+1}=\frac{1}{r_i^2}\left[(J_{i,j}^{n+1/2})^2+\frac{1}{4h_z^2}(\psi_{i,j+1}^{n}-\psi_{i,j-1}^{n})(\psi_{i,j+1}^{n+1}-\psi_{i,j-1}^{n+1})\right]$$
$$+\frac{1}{2r_i h_r}[(\psi_{i+1,j}^{n}-\psi_{i-1,j}^{n})E\psi_{i,j}^{n+1}+(\psi_{i+1,j}^{n+1}-\psi_{i-1,j}^{n+1})E\psi_{i,j}^{n}]$$
$$i=2,\ldots,N_r-1,\quad j=2,\ldots,N_z-1 \tag{18}$$

Equations (17)–(18) are coupled by the boundary conditions in the following form:

$$\begin{aligned}
&\frac{\psi_{2,j}^{n+1}+\psi_{1,j}^{n+1}}{2}=0,\quad \frac{\psi_{2,j}^{n+1}-\psi_{1,j}^{n+1}}{h_r}=0\\
&\frac{\psi_{N_r,j}^{n+1}+\psi_{N_r-1,j}^{n+1}}{2}=0,\quad \frac{\psi_{N_r,j}^{n+1}-\psi_{N_r-1,j}^{n+1}}{h_r}=0 \qquad j=2,\ldots,N_z-1\\
&\frac{\psi_{i,2}^{n+1}+\psi_{i,1}^{n+1}}{2}=0,\quad \frac{\psi_{i,2}^{n+1}-\psi_{i,1}^{n+1}}{h_z}=0\\
&\frac{\psi_{i,N_z}^{n+1}+\psi_{i,N_z-1}^{n+1}}{2}=0,\quad \frac{\psi_{i,N_z}^{n+1}-\psi_{i,N_z-1}^{n+1}}{h_z}=0 \qquad i=2,\ldots,N_r-1
\end{aligned} \tag{19}$$

To combine Equations (17)–(19) as a *single* linear system with banded matrix we introduce new system of indices as follows:

$$k_{(i,j)}=2(i-1)N_z+2j-1,\quad i=1,\ldots,N_r$$
$$m_{(i,j)}=2(i-1)N_z+2j=k_{(i,j)}+1,\quad j=1,\ldots,N_z$$

Copyright © 2009 John Wiley & Sons, Ltd.

DOI: 10.1002/fld

Each node (i, j) of the grid Q_h is associated with two indices $k_{(i,j)}$ and $m_{(i,j)}$. Index $k_{(i,j)}$ is an odd number and index $m_{(i,j)}$ is an even number. It is easy to see that

$$\begin{aligned} k_{(i+1,j)} &= k_{(i,j)} + 2N_z, \quad k_{(i,j+1)} = k_{(i,j)} + 2 \\ k_{(i-1,j)} &= k_{(i,j)} - 2N_z, \quad k_{(i,j-1)} = k_{(i,j)} - 2 \end{aligned} \tag{20a}$$

$$\begin{aligned} m_{(i+1,j)} &= m_{(i,j)} + 2N_z, \quad m_{(i,j+1)} = m_{(i,j)} + 2 \\ m_{(i-1,j)} &= m_{(i,j)} - 2N_z, \quad m_{(i,j-1)} = m_{(i,j)} - 2 \end{aligned} \tag{20b}$$

Now we introduce a new grid function σ_k, which is defined on the composite grid. Here, σ_k represents $\psi_{i,j}$ and σ_m represents $\Phi_{i,j}$. Substituting σ_k and σ_m *in lieu* of $\psi_{i,j}$ and $\Phi_{i,j}$ in the Equations (17)–(18), we recast the algebraic system as the following:

$$\begin{aligned} &\frac{\sigma_k^{n+1} - \sigma_k^n}{\tau} - \frac{1}{8 r_i h_r h_z}[(\sigma_{k+2N_z}^n - \sigma_{k-2N_z}^n)(\sigma_{k+2}^{n+1} - \sigma_{k-2}^{n+1}) + (\sigma_{k+2N_z}^{n+1} - \sigma_{k-2N_z}^{n+1}) \\ &\quad \times (\sigma_{k+2}^n - \sigma_{k-2}^n)] + \frac{1}{2h_z}(\sigma_{k+3}^{n+1} - \sigma_{k-1}^{n+1}) = \frac{1}{2}(E\sigma_k^{n+1} + E\sigma_k^n) \end{aligned} \tag{21a}$$

$$\begin{aligned} E\sigma_m^{n+1} &= \frac{1}{r_i}\left[(J_{i,j})^2 + \frac{1}{4h_z^2}(\sigma_{m+1}^n - \sigma_{m-3}^n)(\sigma_{m+1}^{n+1} - \sigma_{m-3}^{n+1})\right] \\ &\quad + \frac{1}{r_i}\left[\frac{(\sigma_{m+2N_z-1}^n - \sigma_{m-2N_z-1}^n)}{2h_r} E\sigma_{m-1}^{n+1} + \frac{(\sigma_{m+2N_z-1}^{n+1} - \sigma_{m-2N_z-1}^{n+1})}{2h_r} E\sigma_{m-1}^n\right] \end{aligned} \tag{21b}$$

where

$$E\sigma_k = \frac{(\sigma_{k+2N_z} - 2\sigma_k + \sigma_{k-2N_z})}{h_r^2} - \frac{(\sigma_{k+2N_z} - \sigma_{k-2N_z})}{2r_i h_r} + \frac{(\sigma_{k+2} - 2\sigma_k + \sigma_{k-2})}{h_z^2}$$

Since the boundary conditions (19) are homogeneous, the straightforward implementation of the algorithm leads to a problem with a singular matrix. There are different ways to regularize the problem. We found that adding a small term proportional to ψ at the boundary gives the best results. According to this idea, Equation (19) can be rewritten as follows:

$$\frac{\sigma_k^{n+1} + \sigma_{k+2N_z}^{n+1}}{2} = 0, \quad \frac{\sigma_{m+2N_z-1}^{n+1} - \sigma_{m-1}^{n+1}}{h_r} = 0, \quad i = 1, \ \ j = 1, \ldots, N_z \tag{22a}$$

$$\frac{\sigma_k^{n+1} + \sigma_{k-2N_z}^{n+1}}{2} = 0, \quad \frac{\sigma_{m-1}^{n+1} - \sigma_{m-2N_z-1}^{n+1}}{h_r} = 0, \quad i = N_r, \ \ j = 1, \ldots, N_z \tag{22b}$$

$$\frac{\sigma_k^{n+1} + \sigma_{k+2}^{n+1}}{2} = 0, \quad \frac{\sigma_{m+1}^{n+1} - \sigma_{m-1}^{n+1}}{h_z} = \varepsilon\sigma_m^{n+1}, \quad j = 1, \ \ i = 1, \ldots, N_r \tag{22c}$$

$$\frac{\sigma_k^{n+1} + \sigma_{k-2}^{n+1}}{2} = 0, \quad \frac{\sigma_{m-1}^{n+1} - \sigma_{m-3}^{n+1}}{h_z} = \varepsilon\sigma_m^{n+1}, \quad j = N_z, \ \ i = 1, \ldots, N_r \tag{22d}$$

where ε is a very small number.

Copyright © 2009 John Wiley & Sons, Ltd.

DOI: 10.1002/fld

The above-described scheme allows one to compute any kind of transient unsteady regimes of the flow under consideration. If the steady flow is the aim, then the algorithm can be considered as an iterative procedure and the time steps are terminated at certain $n=N$ when the following criterion is satisfied:

$$\frac{\max\limits_{i,j}|\mathbf{f}_{i,j}^{N+1}-\mathbf{f}_{i,j}^{N}|}{\max\limits_{i,j}|\mathbf{f}_{i,j}^{N+1}|}\leqslant 10^{-6}$$

where $\mathbf{f}_{i,j}=\{\sigma_{i,j},\ \ J_{i,j}\}$ is the vector of all unknown variables at a given point of the grid.

Note that the linear system for the coupled formulation of the $\psi-\Phi$ problem can be written as the following multi-diagonal system for the composite grid function σ

$$\begin{aligned}&B_{l,l-2N_z-1}\sigma_{l-2N_z-1}^{n+1}+B_{l,l-2N_z}\sigma_{l-2N_z}^{n+1}+B_{l,l-3}\sigma_{l-3}^{n+1}+B_{l,l-2}\sigma_{l-2}^{n+1}\\&\quad+B_{l,l-1}\sigma_{l-1}^{n+1}+B_{l,l}\sigma_{l}^{n+1}+B_{l+1}\sigma_{l+1}^{n+1}+B_{l,l+2}\sigma_{l+2}^{n+1}\\&\quad+B_{l,l+2N_z-1}\sigma_{l+2N_z-1}^{n+1}+B_{l,l+2N_z}\sigma_{l+2N_z}^{n+1}+B_{l,l+2N_z+1}\sigma_{l+2N_z+1}^{n+1}=F_l\end{aligned}\tag{23}$$

where $l=1,\ldots,2N_zN_r$. The matrix of the algebraic system Equation (23) is banded with $2N_z+1$ lower and $2N_z+1$ upper diagonals. We used standard routines `DGBSV` and `DGBSVX` of the `LAPACK` to solve Equation (23).

Naturally, before doing anything else, we studied thoroughly the impact of the small parameter ε on the results. We computed the condition number, N_{cond}, of the matrix of Equation (23) using the routine `DGBSVX` of `LAPACK` and found that the $N_{\mathrm{cond}}\approx 10^3/\varepsilon$ in the range $\varepsilon\in[10^{-14},10^{-4}]$.

Clearly, there is a trade-off in selecting the value of ε. It is desirable to take it very small but then the condition number will become intolerably large. In order to estimate the optimal ε, we ran computations with several different ε's. The results are summarized in Table I, where the dependence on ε of the maximal and minimal components of the solution are represented. One can see that variations of ε in the range 10^{-10}–10^{-6} have no impact on the computed quantities within four to five significant digits. This kind of accuracy is much better than the truncation error of the scheme and it is a small price to pay for removing the singularity of the matrix.

Table I. Effect of parameter ε on numerical solution for grid 22×42. $\Omega_{\mathrm{u}}=1$, $\eta=2$, $\Gamma=2$, $Re=80$.

Ω	ε	$\psi_{\min}$	$\psi_{\max}$	$\Phi_{\min}$	$\Phi_{\max}$	$J_{\min}$	$J_{\max}$
0	10^{-2}	−3.68293	3.68293	−87.1066	142.977	−39.9864	120.014
	10^{-4}	−3.37555	3.37555	−95.6708	140.492	−40.3144	119.688
	10^{-6}	−3.37560	3.37560	−96.6644	132.361	−40.3143	119.686
	10^{-8}	−3.37555	3.37555	−96.6659	132.378	−40.3144	119.686
	10^{-10}	−3.37555	3.37555	−96.6612	132.477	−40.3144	119.686
1	10^{-2}	−6.53545	6.53545	−322.564	110.315	−150.655	473.445
	10^{-4}	−7.97748	7.97748	−422.439	190.444	−155.980	468.120
	10^{-6}	−7.97720	7.97720	−425.924	160.543	−155.978	468.122
	10^{-8}	−7.97748	7.97748	−425.944	160.554	−155.980	468.120
	10^{-10}	−7.97748	7.97748	−425.947	160.573	−155.980	468.120

Copyright © 2009 John Wiley & Sons, Ltd.

DOI: 10.1002/fld

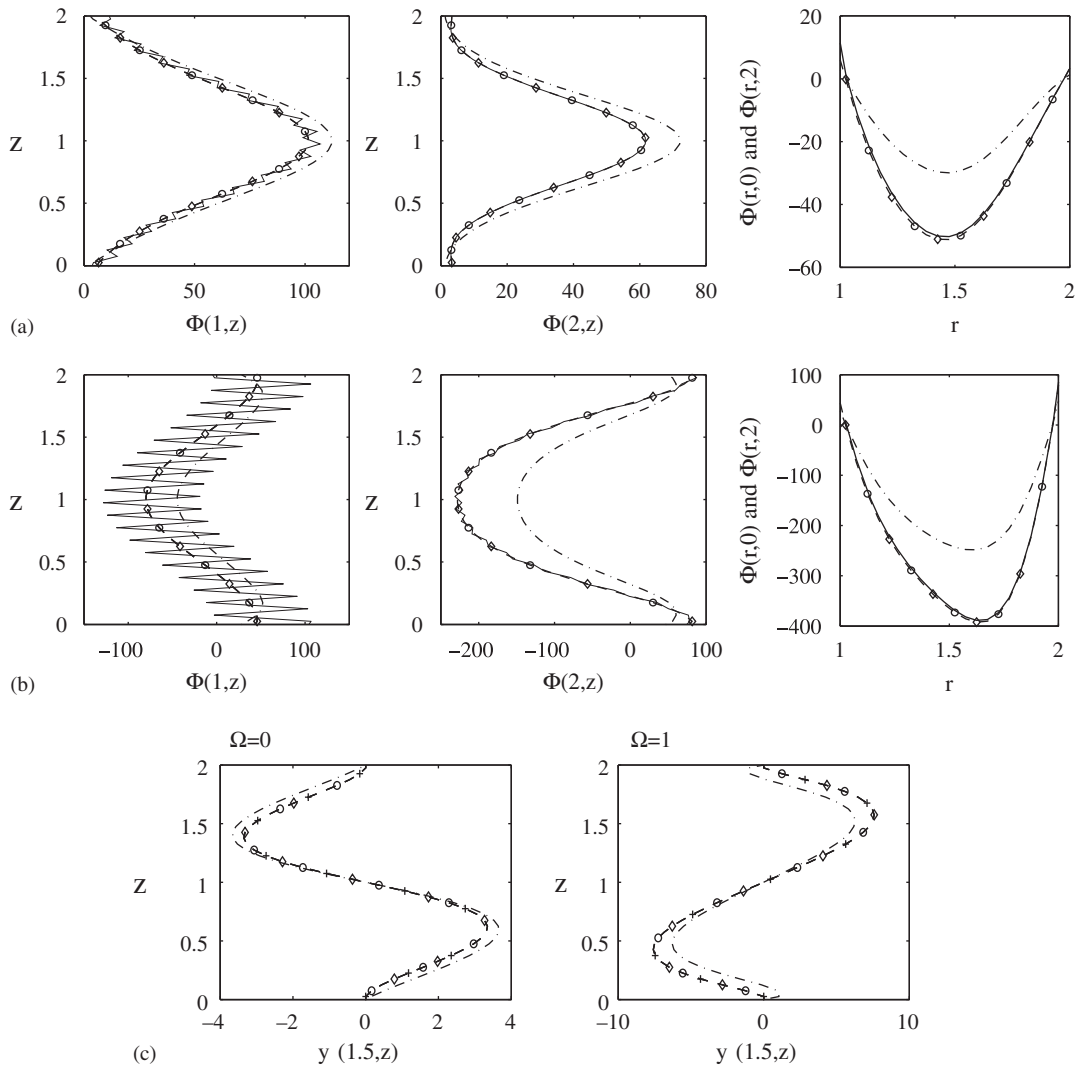

Figure 3. Effect of ε on solution at the boundary. $Re=80, \eta=2$, and $\Gamma=2$: (a) function Φ for $\Omega=0$; (b) function Φ for $\Omega=1$; and (c) stream function ψ.

An additional insight into the impact of ε can be obtained from the results presented in Figure 3 for the values of Φ and ψ at the flow boundaries. In Figure 3, dash-dotted lines correspond to $\varepsilon=10^{-2}$, dashed lines with diamond signs represent $\varepsilon=10^{-6}$, dashed lines with circle signs represent case $\varepsilon=10^{-10}$, and solid lines correspond to $\varepsilon=10^{-14}$. Note that the values $\varepsilon<10^{-10}$ correspond to N_{cond}^{-1} that is lesser than the round-off error. The results for the very small ε are not practical and are presented here for the sake of completeness. One can observe from Figure 3(b) that if $10^{-10}\leqslant\varepsilon\leqslant10^{-6}$, the variations of Φ at the boundaries are negligible. If ε is too small, say, $\varepsilon\leqslant10^{-12}$, then Φ oscillates near the 'correct' values (left panel of Figure 3(b)). It is interesting to

Copyright © 2009 John Wiley & Sons, Ltd.

DOI: 10.1002/fld

Table II. Results of simulation on different grids for $Re=80$, $\Omega=0$, $\eta=2, \Gamma=2$.

$M_r \times N_z$	$\max_{i,j} \lvert\psi_{i,j}\rvert$	Rate
12×22	0.04000	
22×42	0.04219	2.50069
42×82	0.04257	2.38466
62×122	0.04266	

note that more significant oscillations were observed only at the boundary of the inner cylinder. Figure 3(c) shows the values of stream function versus z for $r=1.5$ and $\Omega=0$ and 1, ε varies from 10^{-2} to 10^{-14} (lines with cross signs correspond to $\varepsilon=10^{-14}$). One can see that for $\varepsilon\in[10^{-14}, 10^{-6}]$ the values of stream function change less than 1%.

To estimate the rate of convergence, the solution is obtained on a sequence of grids with 12×22, 22×42, 42×82, and 62×122 nodes. The finest grid is used as a reference solution (pseudo-analytical solution). Then the rate of convergence is computed using two grids according to the formula

$$\text{rate}_1=\ln_2\frac{|\max\psi^{12\times 22}-\max\psi^{62\times 122}|}{|\max\psi^{22\times 42}-\max\psi^{62\times 122}|},\quad \text{rate}_2=\ln_2\frac{|\max\psi^{22\times 42}-\max\psi^{62\times 122}|}{|\max\psi^{42\times 82}-\max\psi^{62\times 122}|} \tag{24}$$

Since we have four grids, we can get two different estimates of the rate. As shown in Table II for one particular choice of the parameters, the two numerically estimated rates, Equation (24), are close to the theoretically predicted second rate of convergence. The interesting thing is that both rates are somewhat better than the theoretical but the tendency is toward approaching the latter. Apparently the coarsest grid 12×22 is not adequate enough.

The results of this section suffice to claim that both the new formulation [5] and its numerical implementation offer a valid approach toward the numerical investigation of rotating flows.

5. RESULTS AND COMPARISONS

In this section we apply the developed numerical tool for investigating the mechanisms of the Taylor–Couette flow for different values of the governing parameters.

5.1. Role of the relative angular speed Ω of the lids

As mentioned above, we consider the case when both lids rotate with the same angular velocity Ω_e, while the outer cylinder is held at rest. The ratio $\Omega=\Omega_e/\Omega_i$ is one of the main governing parameters of the problem. It is important to investigate the bifurcation and emergence of a secondary streaming in the vertical plane for different values of Ω. In this subsection, we fix $\eta=2$, $Re=80$, $\Gamma=2$, and vary Ω. The results are obtained for each case beginning from the solution for $Re=0$ and then gradually increasing the Reynolds number up to the selected value $Re=80$. The way of varying the Reynolds number is important because the problem is nonlinear and presents a classical case of hysteresis: the result depends on the route chosen to obtain it. The hysteresis will be treated in Section 5.3.

Copyright © 2009 John Wiley & Sons, Ltd.

DOI: 10.1002/fld

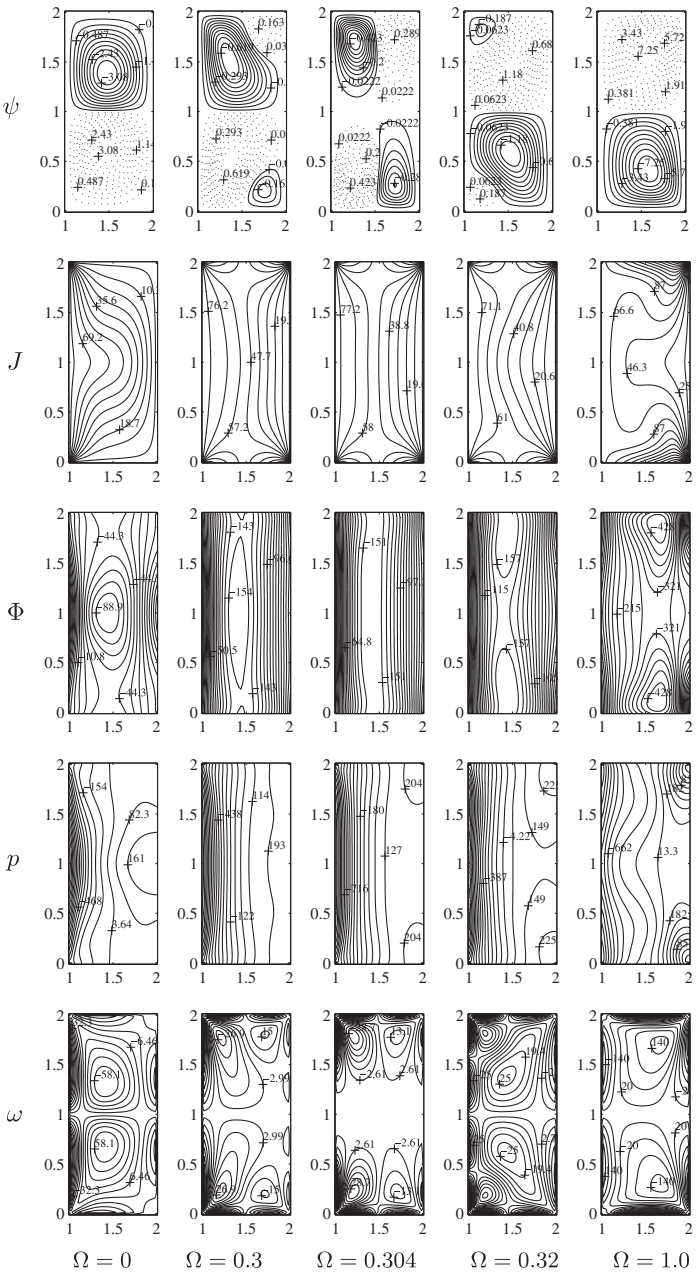

Figure 4. Contour plots of stream function ψ, azimuthal velocity component $J = rv$, function Φ, pressure p, and vorticity ω for $\Gamma = 2$, $Re = 80$, $\eta = 2$.

Copyright © 2009 John Wiley & Sons, Ltd.

DOI: 10.1002/fld

Table III. Comparison of $\psi_{\max}$ for the $\Omega=0, 0.3, 0.304, 0.32, 1$ and $Re=80, \eta=2, \Gamma=2$.

Ω	0	0.3	0.304	0.32	1
Present (42×82)	0.04257	0.00855	0.00584	0.01636	0.10010
Reference [6]	0.04270	0.00869	0.00578	0.01667	0.10014

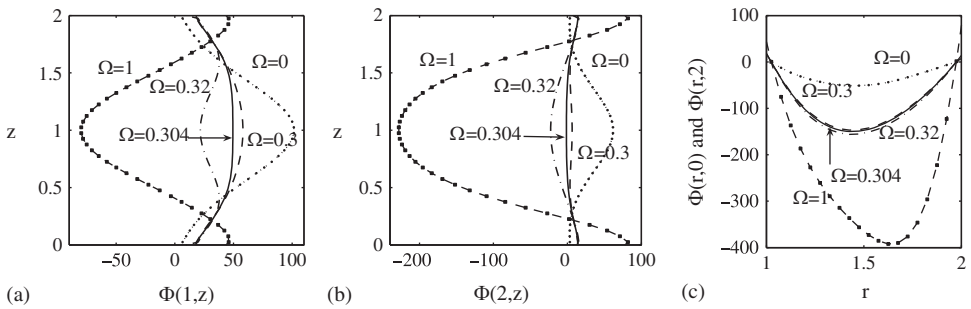

Figure 5. Boundary profiles of Φ for $Re=80, \eta=2, \Gamma=2$, and different Ω's.

The results from our computations are presented in Figure 4. The first row of drawings gives the streamlines in the (r, z)-plane, the second row—isolines of azimuthal function J, the third row shows the isolines of Φ, the fourth row shows the lines of constant pressure p, the last (fifth) row presents the isolines of vorticity ω. Note that the vorticity and pressure are computed from ψ and Φ after the iterations converge. The streamline patterns are in excellent agreement with the results of [6].

As mentioned in [6], when $\Omega=0$, the flow regime is characterized by an inward flow adjacent to both of the lids and a narrow jet in the axial mid-plane flowing toward the outer cylinder. If the lids rotate synchronously with the inner cylinder ($\Omega=1$), a different regime appears. The direction of flow is opposite to that in the case of $\Omega=0$. When the relative rotation rate of the lids, Ω, is increased from zero to one, one of the patterns gradually morphs into the other. Our computational experiments shown that the flow pattern changes qualitatively in the range of $\Omega\in[0.3, 0.32]$, which is in agreement with [6]. The maximum values of stream function are given in Table III. They are in close agreement with the computational and experimental data [6].

Function Φ is the most sensitive function in the numerical computations, and it reveals some deeper mechanisms of the rotational flow. We find it important to understand better the behavior of this function for Ω's in the interval where the transformation of the flow regime occurs. We present in Figure 5, the boundary distribution of Φ as a function of the vertical coordinate z (left and middle panels) and as a function of the radial coordinate r (right panel).

In the case $\Omega=0$ (the lids do not rotate), the function Φ has positive maximum in the middle of the vertical wall ($z=1$). For $\Omega=1$ (the lids rotate simultaneously with inner cylinder), Φ has negative minimum. Thus, we see that the boundary profiles of Φ change dramatically for those Ω for which the streamline patterns change.

We continue with the examination of the 2D profile of Φ shown in Figure 6. One can see that while for $\Omega=0$, the profile is more like a cup, with the increase of Ω it transforms first into an

Copyright © 2009 John Wiley & Sons, Ltd.

DOI: 10.1002/fld

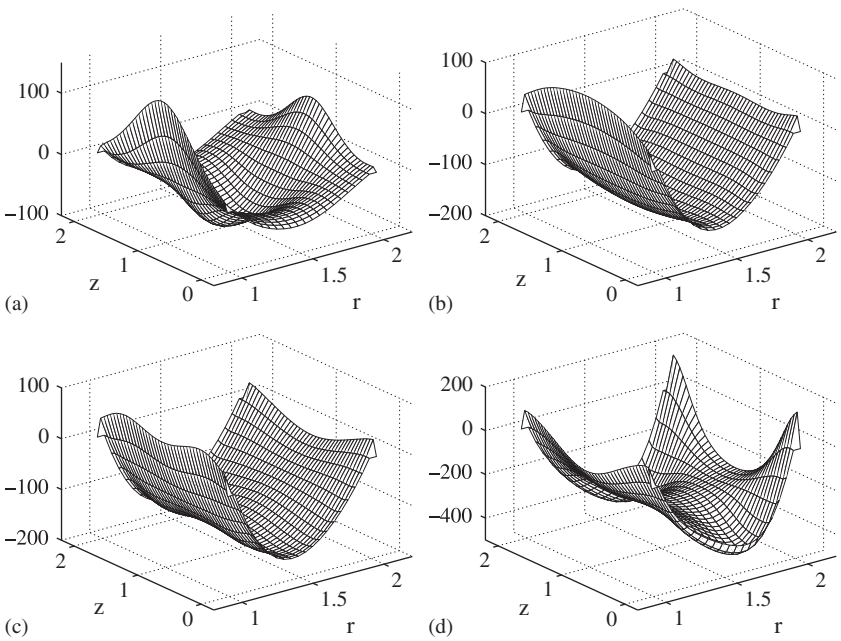

Figure 6. Surface plots of Φ for $Re=80, \eta=2$, and $\Gamma=2$ and four different values of Ω: (a) $\Omega=0$; (b) $\Omega=0.3$; (c) $\Omega=0.32$; and (d) $\Omega=1$.

almost cylindrical surface (in the region $\Omega\in[0.3, 0.32]$ of appearance of the four-eddy solution) and eventually adopts a saddle shape for $\Omega=1$.

5.2. *Role of the aspect ratio* Γ

The dynamics of the flow when driven by the rotation of the inner cylinder and the bottom lid only ($\Omega_u=0, \Omega=1$), was investigated in [14] for $Re\in[100, 200]$, $\Gamma\in[2.5, 3.25]$, and $\eta=2$. It was pointed out there that for $Re=100$ and small to moderate Γ, the flow consists of a single cell, created essentially by the rotation of the bottom lid. As the relative length Γ increases, the one-eddy stationary flow is eventually replaced by a three-eddy structure. It is important to apply the tool developed here for the investigation of the transformation of secondary streaming for $\Omega_u=0$. To compare with the experiments we select $Re=100$ and $\eta=2$ and vary Γ. Figure 7 presents our result for the transformation of the secondary flow with increasing Γ.

We have found that a sole vortex appears in the secondary streaming for $\Gamma<2.5$. Since the inner cylinder is rotating, the vortex cannot split into two counter-rotating eddies, hence for $\Gamma=2.5$ and $\Gamma=2.7$, a pattern known as 'Kelvin's cat's eye' develops. If it were a primary flow, the appearance of the cat's eye is a clear indication of pending instability, but in secondary streaming, it is quite a standard situation to have a streaming of a type of *cat's eye* (see, for instance [15] for the flow in rotating annulus and [16] for the secondary flow in the cross section of a curved pipe).

The further increase of the aspect ratio to $\Gamma=2.8$ leads to 'pinching' the vortex of the secondary streaming and $\Gamma=2.81$ marks the actual transition to a three-eddy structure, when the small third eddy occurs between the two eyes of the *cat's eye* and spans with the increase of Γ the entire

Copyright © 2009 John Wiley & Sons, Ltd.

DOI: 10.1002/fld

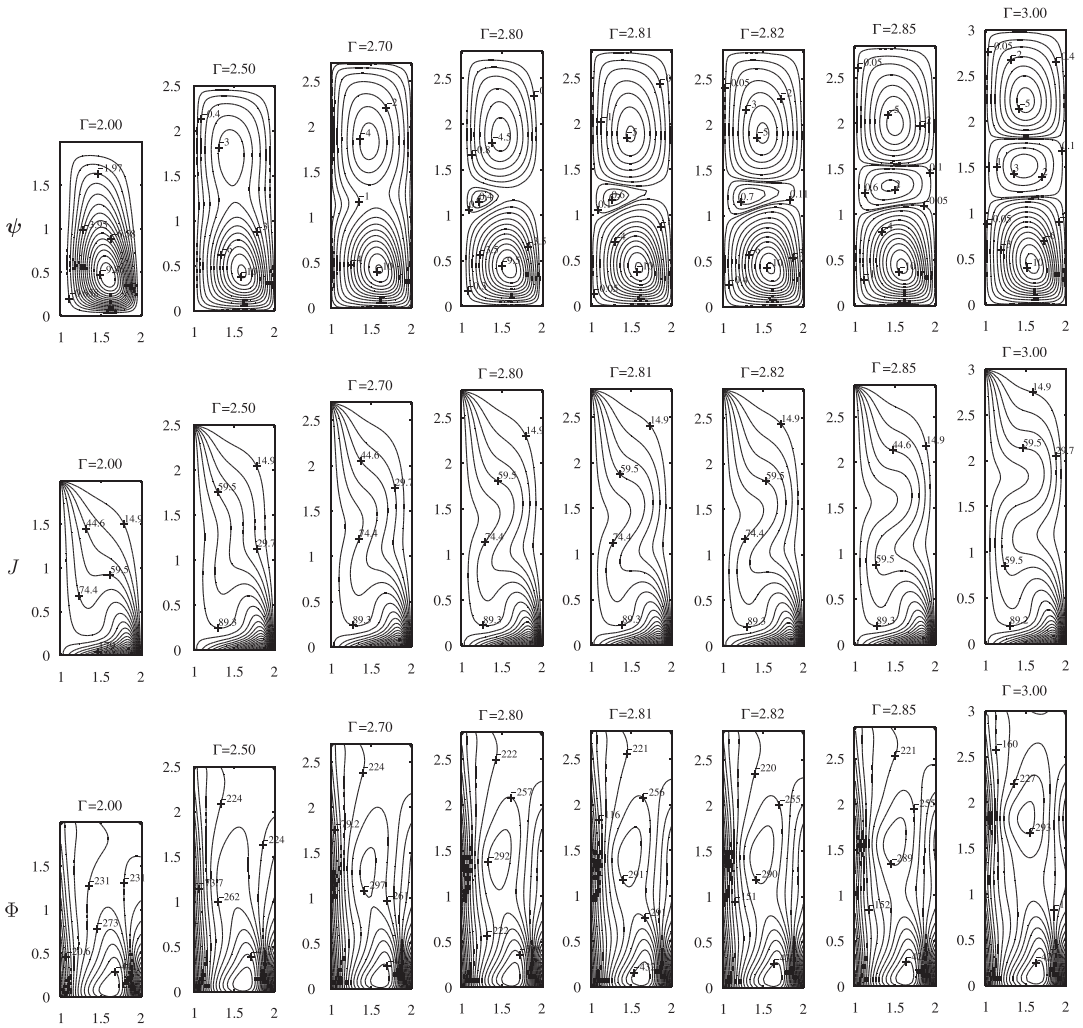

Figure 7. Sequence of the steady axisymmetric solutions for $Re = 100$ for different Γ.

breath of the gap. As it should have been expected, the further increase of Γ allows the third eddy to grow and to become commensurate with the other two.

Once again, function Φ manifests itself as a characteristic that is very sensitive to qualitative changes. Even before the third eddy becomes visible in the flow pattern, Φ develops a minimum approximately in the same region where the third eddy is about to appear. The position of the minimum moves up with the expansion of the third eddy.

Note that the results in Figure 7 are obtained with initial conditions that are the flow fields for the previous (smaller) value of Γ. For the relatively low Reynolds number, $Re = 80$, we did not discover a hysteresis effect, which is expected to appear when the nonlinearity dominates the dynamics.

Copyright © 2009 John Wiley & Sons, Ltd.

DOI: 10.1002/fld

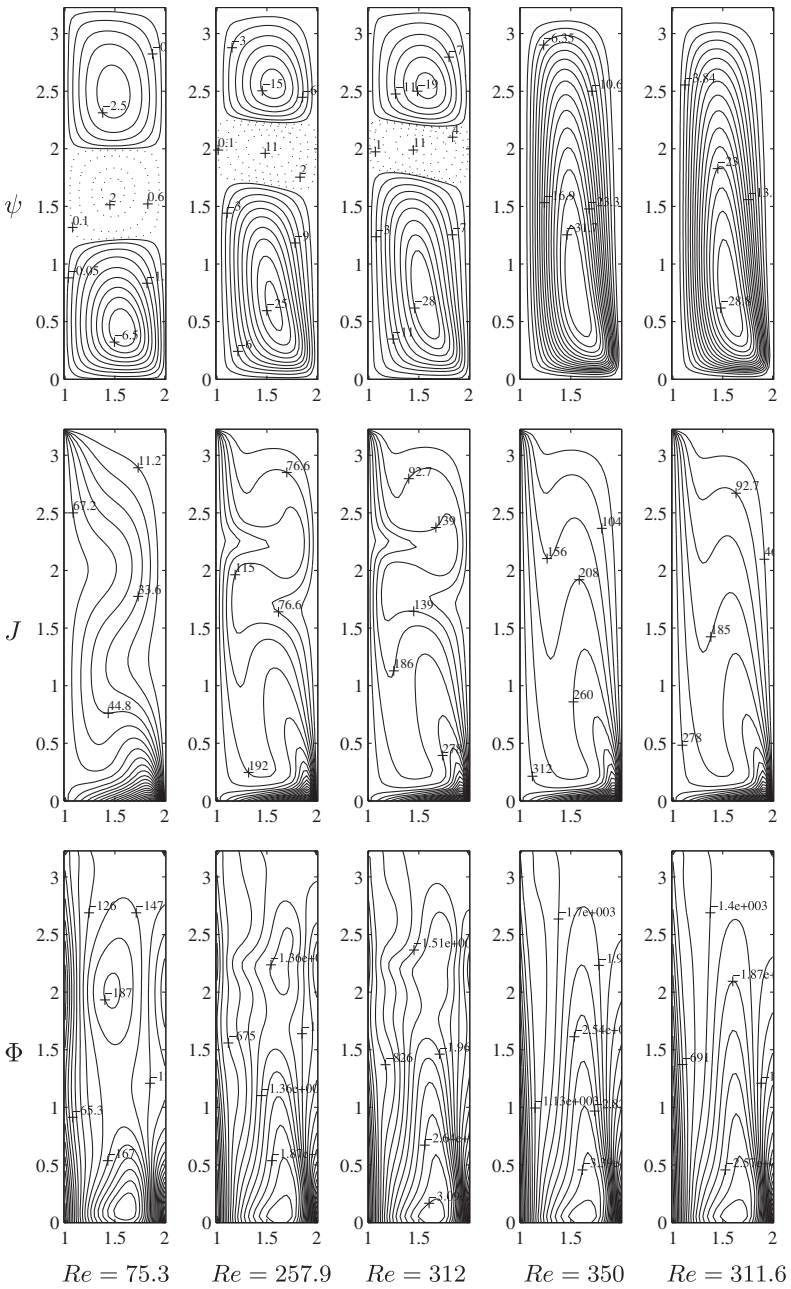

Figure 8. Sequence of flow pattern with different Re for $\Gamma = 3.226$, $\eta = 2$.

Copyright © 2009 John Wiley & Sons, Ltd.

DOI: 10.1002/fld

5.3. Role of Reynolds number Re and hysteresis

In order to understand better the role of nonlinearity in the process of transition from a two-eddy to a three-eddy secondary streaming, we chose $\Gamma=3.226$ which lies securely inside the region of parameters where the three-eddy structure is to be expected. For consistency, we consider the same $\eta=2$ when the bottom lid and the inner cylinder rotate together ($\Omega=1$), while the upper lid and the outer cylinder are at rest. Experimental and numerical studies of this particular Taylor–Couette flow were conducted in [9, 14]. In the experiments of [9], for a fixed aspect ratio, observations of the flow with different Reynolds number were performed. Beginning with certain critical Re, a saddle-node bifurcation was discovered, which brings into existence a single cell flow.

We utilized our algorithm to compute a 'typical' sequence of steady-state patterns for the same parameters as those used in [9]. After the flow is established for a particular Reynolds number (say, Re_0), we increase Re in small increments according to the formula $Re=Re_0(1-\exp(-0.05(n-1)))$, where $n=1,2,\ldots,n_f$ is the time step. The number n_f defines the value of Re, which has to be reached. Then we continue the time steps $n>n_f$ with the last value of the Reynolds number until stationary regime is attained. Thus, we are able to proceed from one Reynolds number to another without imposing discontinuous initial condition. These precautions are needed in order to avoid artificial jumps that can make the solution end up in another bifurcated state.

The steady states that we were able to reach with this algorithm are shown in Figure 8. As usual, we show the stream function in the first row, the azimuthal function—in the second row, and Φ-function—in the third. By slowly increasing Re we reached $Re=350$ for which Reynolds number the flow changed from a three-eddy structure to a single eddy. The interesting property that is observed in this series of computations is the hysteresis. Now, beginning with $Re=350$ we started gradually decreasing the Reynolds number according to the rule $Re=350-38.4(1-\exp(-0.05(n-1)))$, and found that the one-eddy solution exists in the region where the three-eddy solution also exists. Coming down from a higher Re, the smallest Re for which we found a one-eddy solution was $Re=311.6$. The grid consisted of 32×62 nodes and time increment was $\tau=0.001$. The results of our numerical experiments compare quantitatively very well with the case presented in [9], where results of numerical simulations are compared with results of physical experiments.

6. CONCLUSION

The new formulation for axisymmetric Navier–Stokes flows proposed by Aristov and Pukhnachev [5], is implemented numerically. The approximations for the different functions are staggered in time. Thus, the equation for the azimuthal velocity component is decoupled from the rest of the equations and is approximated on fractional time steps. The equations for the stream function, ψ, and the new unknown function of Aristov–Pukhnachev's formulation, Φ, are considered as a coupled system at full time steps. The coupling for the latter system is crucial because of the lack of boundary conditions for the new function and the presence of two boundary conditions for the stream function. Upon renumbering the grid points in a hopscotch manner, the coupled system is formulated as a single system and solved by a `LAPACK` algorithm.

The main difficulty with this formulation is that the coupled system for ψ and Φ is singular. To avoid the singularity, part of the Neumann boundary conditions for the composite function

Copyright © 2009 John Wiley & Sons, Ltd.

DOI: 10.1002/fld

is replaced by Robin boundary conditions with a small parameter multiplying the function. The result is that the originally infinite condition number of the system behaves as $1000\varepsilon^{-1}$ and even for very small $\varepsilon \propto 10^{-10}$, the Gaussian elimination is perfectly stable. The impact on the results of the actual value of the artificial small parameter is judiciously evaluated by numerical experiments and shows that for $\varepsilon \propto 10^{-6}$, the results are correct within six significant digits, which is much better than the truncation error.

The new numerical model is applied to the flow between two rotating cylinders when the lids are also allowed to rotate. This particular Taylor–Couette flow exhibits a rich phenomenology depending on the relative rotations of the lids. We show that the new technique performs robustly and allows one to follow accurately the rearrangement of the flow patterns with the changes of the relative rotation of the lids, Ω. The results are in good quantitative agreement with [6, 9, 14] in the common ranges of the main parameters.

The present paper shows that the Aristov–Pukhnachev's formulation is a viable approach to axisymmetric Navier–Stokes flows and can serve as a basis for efficient numerical models.

REFERENCES

1. Lopez JM. Axisymmetric vortex breakdown part 1. Confined swirling flow. *Journal of Fluid Mechanics* 1990; **221**:533–552.
2. Brown GL, Lopez JM. Axisymmetric vortex breakdown part 2. Physical mechanisms. *Journal of Fluid Mechanics* 1990; **221**:553–576.
3. Lopez JM, Perry AD. Axisymmetric vortex breakdown part 3. Onset of periodic flow and chaotic advection. *Journal of Fluid Mechanics* 1992; **234**:449–471.
4. Abshagen J, Lopez JM, Marques F, Pfister G. Symmetry breaking via global bifurcations of modulated rotating waves in hydrodynamics. *Physical Review Letters* 2005; **94**(7):074501.
5. Aristov SN, Pukhnachev VV. On the equations of axisymmetric motion of a viscous incompressible. *Doklady Physics* 2004; **49**(2):112–115.
6. Abshagen J, Cliffe KA, Langenberg J, Mullin T, Pfister G, Tavener SJ. Taylor–Couette flow with independently rotating end plates. *Theoretical and Computational Fluid Dynamics* 2004; **18**(2–4):129–136.
7. Youd AJ, Barenghi CF. Reversing and nonreversing modulate Taylor–Couette flow at finite aspect ratio. *Physical Review E* 2005; **72**:056321.
8. Inamuro T, Yamaguchi A, Ogino F. Fluid flow in a rotating cylindrical container with a rotating disk at the fluid surface. *Fluid Dynamics Research* 1997; **21**:417–430.
9. Mullin T, Blohm C. Bifurcation phenomena in a Taylor–Couette flow with asymmetric boundary conditions. *Physics of Fluids* 2001; **13**(1):136–140.
10. Mullin T, Toya Y, Tavener SJ. Symmetry breaking and multiplicity of states in small aspect ratio Taylor–Couette flow. *Physics of Fluids* 2002; **14**(8):2778–2787.
11. Pfister G, Schmidt H, Cliffe KA, Mullin T. Bifurcation phenomena in Taylor–Couette flow in a very short annulus. *Journal of Fluid Mechanics* 1988; **191**:1–18.
12. Smagulov Sh, Christov CI. Iterationless numerical implementation of the boundary conditions in vorticity–stream function formulation of Navier–Stokes equations. *Preprint 20*, Institute of Theoretical and Applied Mechanics, Russian Academy of Science, Novosibirsk, 1980; In Russian.
13. Marinova RS, Christov CI, Marinov TT. A fully coupled solver for incompressible Navier–Stokes equations using coordinate operator splitting. *International Journal of Computational Fluid Dynamics* 2003; **17**:371–385.
14. Lopez JM, Marques F, Shen J. Complex dynamics in a short annular container with rotating bottom and inner cylinder. *Journal of Fluid Mechanics* 2004; **501**:327–354.
15. Solomon TH, Holloway WJ, Swinney HL. Shear flow Instabilities and Rossby waves in barotropic flow in a rotating annulus. *Physics of Fluids A* 1993; **5**(8):1971–1982.
16. Zapryanov Z, Christov C. Fluid flow and heat transfer in toroidal tubes. *Advances in Mechanics* 1980; **3**(4):55–90 (in Russian).

Copyright © 2009 John Wiley & Sons, Ltd.

DOI: 10.1002/fld